



In vivo PS-OCT needle probe scan of human skeletal muscle

JEFFREY M. MCBRIDE,^{1,2,6,*} MICHAEL J. HACKMANN,^{3,4,6} SOPHIA NIMPHIUS,² AND BARRY CENSE^{4,5} 

¹Department of Health & Exercise Science, Appalachian State University, Boone, NC 28608, USA

²School of Medical and Health Sciences, Edith Cowan University, Joondalup, 6027, Australia

³School of Human Sciences, The University of Western Australia, Crawley, WA, Australia

⁴Department of Electrical, Electronic and Computer Engineering, University of Western Australia, Perth, 6009, Australia

⁵Department of Mechanical Engineering, Yonsei University, Seoul, 03722, Republic of Korea

⁶Contributed equally

*mcbridejm@appstate.edu

Abstract: Polarization-sensitive optical coherence tomography (PS-OCT) derived birefringence values effectively identify skeletal muscle structural disruption due to muscular dystrophy and exercise-related muscle damage in animal models in *ex vivo* tissue. The purpose of this investigation was to determine if a PS-OCT needle probe inserted into the leg of a human subject could accurately identify various anatomical structures with implications for use as a diagnostic tool for the determination of skeletal muscle pathology. A healthy middle-aged subject participated in this study. A custom-built PS-OCT system was interfaced with a side-viewing fiber-optic needle probe inserted into the subject's vastus lateralis muscle via a motorized stage for 3D data acquisition via rotation and stepwise pullback. The deepest recorded PS-OCT images correspond to a depth of 6 mm beneath the dermis with structural images showing uniform, striated muscle tissue. Multiple highly birefringent band-like structures with definite orientation representing connective tissue of the superficial aponeurosis appeared as the depth of the needle decreased. Superficial to these structures the dominating appearance was that of adipose tissue and low birefringent but homogeneous scattering tissue. The data indicate that a PS-OCT needle probe can be inserted into live human skeletal muscle for the identification of relevant anatomical structures that could be utilized to diagnose significant skeletal muscle pathology.

© 2022 Optica Publishing Group under the terms of the [Optica Open Access Publishing Agreement](#)

1. Introduction

Current clinical practice for assessment of muscular dystrophy involves painful, time-consuming, and costly punch biopsies, which require extensive processing before data are available. As an alternative, optical birefringence measurements have been employed to examine skeletal muscle structure [1]. This approach leverages the link between optical properties and tissue ultrastructure. Skeletal muscle cells (myofibers) are thin and elongated (10-50 μm wide and 1-40 mm long) and consist of bundles of parallel packed filaments (1 μm thin myofibrils) interspersed with sarcoplasm [2]. Under the light microscope myofibrils appear striated due to the alternating arrangement bright I-bands (consisting of only thin actin filaments) and dark A-bands (consisting mainly of thick myosin filaments layered with thin actin). The A-bands are named after their anisotropy and are the main contributor to muscular form birefringence. Deterioration of muscular structural integrity causes a loss of the anisotropic ultrastructure and can be assessed through birefringence measurements [3].

In fact, PS-OCT derived birefringence values have been revealed to be effective for identification of skeletal muscle structural disruption as a result of muscular dystrophy and exercise related muscle damage [4,5]. This may be especially useful to identify Duchenne Muscular Dystrophy

(DMD) which is a muscle pathology by which the genetic code necessary for the transcription of the protein dystrophin is absent. The identification of muscle pathology in the above investigations was established by assessing PS-OCT analysis of excised animal muscle tissue to hematoxylin & eosin staining of frozen cross-sections of the corresponding area [4]. However, optical measurements are limited by the penetration depth of light into tissue and cannot readily reach to depths of skeletal muscle, prompting the development of fiber-optic needle probes for deep tissue visualization [6–8]. A consequent study utilized a 30-gauge (310 μm outer diameter) OCT needle probe that was inserted into excised animal skeletal muscle tissue *in vitro* generate 3-D rendered volumetric data sets of muscle structure [5]. Thus, this investigation substantiated the practicality of inserting a needle probe into muscle tissue to obtain valid optical values [5]. However, until now no studies have examined the efficacy of using a PS-OCT needle probe inserted into *in vivo* human skeletal muscle to utilize calculated birefringence values as an assessment of skeletal muscle structural integrity.

2. Method

2.1. Subject

The subject was a healthy aged male (age = 48 years, body mass = 85.9 kg, height = 1.78 m) with no muscular disorders or musculoskeletal injury within the past year. The Institutional Review Board at Edith Cowan University granted ethics approval (#22067) for all methods in this study. Voluntary written consent was obtained from the subject before commencement of any testing.

2.1.1. PS-OCT system and needle probe

A custom-built PS-OCT system was interfaced with a side viewing fiber-optic needle probe mounted on a motorized stage for 3D data acquisition via rotation and stepwise pullback. System and needle have previously separately been described in detail [9–12]. The combined system is shown in Figure 1.

2.2. Data acquisition and -processing

The needle probe was mounted on a motorized rotation- and translation stage fitted with a fiber-optic rotary joint (MJP FAPB 131-28 FA, Princetel Inc., Hamilton, NJ, USA). Following sterilization of the needle and the site of insertion and the application of a topical anesthetic the subject was seated on a medical couch with the left thigh exposed and fixated (Fig. 2). The initial insertion of the needle into the volunteer's left vastus lateralis was then achieved by manual translation without rotation to the desired depth of about 6 mm (depth of the needle's imaging window). For the PS-OCT scan, counter-rotation (back and forth rotation) was performed at 1.25 Hz with pullback steps of 12.5 μm after each left-handed, but not right-handed rotation. The depth-position of the imaging window (and hence the image itself) with respect to the tissue surface (epidermis surface) was reconstructed from the number of pullback steps separating them. The rotation angular range was set to $\pm 490^\circ$ to avoid non-uniform rotation distortion (NURD) artefacts that may appear due to motor angular acceleration or deceleration phases and A-scans corresponding to 360° rotation were cropped from the data. Only images of the same rotation orientation were analyzed, although nearly ideal overlap of tissue features from both rotational directions was observed. This indicates that tissue drag, which may be caused by continuous rotation of the needle and is associated with tissue damage and image distortion, was thereby prevented. In our Jones-matrix PS-OCT system the two orthogonal input states (P and S) and the two orthogonal detection channels (H and V) allow to directly capture the entire round-trip Jones

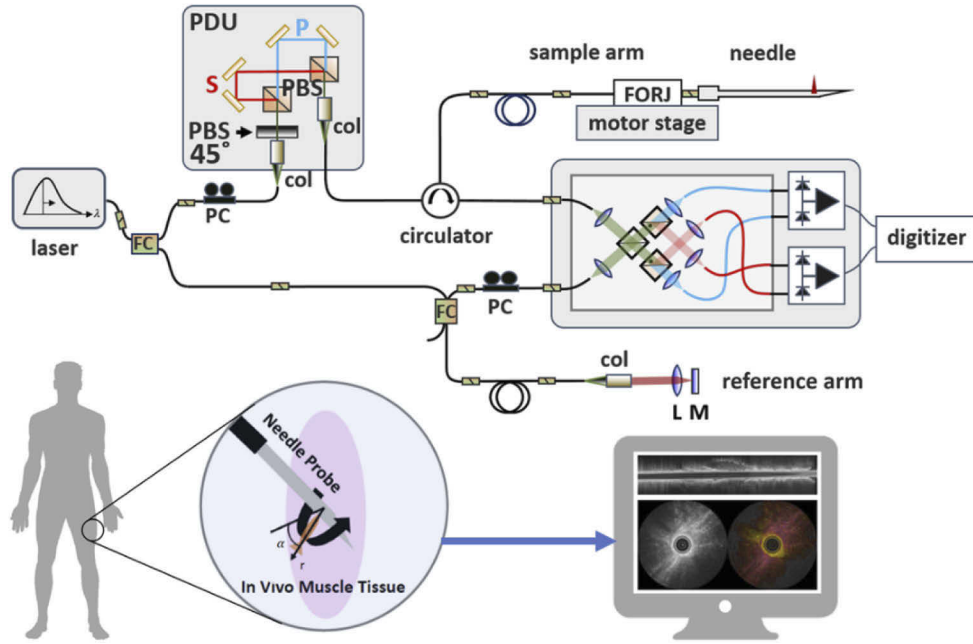


Fig. 1. Schematic of the 1300 nm fiber-based PS-OCT system. The system employs a wavelength-swept laser (AXP50124-8, Axsun Technologies, Bellerica, MA, USA), operating at a central wavelength of 1300 nm with a bandwidth of 130 nm and a repetition rate of 50 kHz. Light is split between reference arm and sample arm by a 90/10 fiber-coupler. In the sample arm two orthogonal linearly polarized input polarization states (P and S) are created and a relative offset is introduced by a polarization delay unit (PDU). At the sample a fiber-optic needle probe delivers 7 mW beam power in a focused beam of $20\ \mu\text{m}$ $1/e^2$ spot diameter (all given values are in tissue). The system's axial resolution of $7\ \mu\text{m}$ is constant over the effective imaging range of 2.9 mm. Light that is backscattered by the tissue carries its polarizing properties and is collected via the needle probe and subsequently relayed to the detection unit, where it is mixed with the reference arm light in a polarization diverse optical mixer (PDOM-1310, Finisar, Sunnyvale, USA) and subsequently detected by a pair of balanced receivers (PDB460C-AC, Thorlabs, USA). The photocurrents are digitized (ATS9350, Alazar Technologies Inc., Pointe-Claire, Québec, Canada) using the laser's k-clock for sampling that is linear in wavenumber and the raw data is continuously written to disk. The needle probe was assembled from a side-viewing monolithic fiber-optical probe encased in a 24-gauge hypodermic needle of $570\ \mu\text{m}$ outer diameter. The optical probe consists of a length of single-mode fiber (SMF-28, Corning Inc., USA) spliced to $280\ \mu\text{m}$ of no-core fiber (NCF125, POFC, Taiwan) to expand the beam before focusing via a $110\ \mu\text{m}$ long segment of GRIN fiber (GIF625, Thorlabs, USA). A side-viewing probe is achieved by adding a short segment of no-core fiber that is angle polished at 48° for total internal reflection and surrounded by a collapsed glass capillary.

matrix for each pixel in the image.

$$J(z) = \begin{bmatrix} t_H^S(z) & t_H^P(z) \\ t_V^S(z) & t_V^P(z) \end{bmatrix} \quad (1)$$

We employ the signal processing algorithms developed by Villiger et al. [11] and Li et al. [9], to compute sample birefringence and optic axis orientation, respectively, after correcting for transmission through fiber and system components [9] and the effects of the rotating optical probe

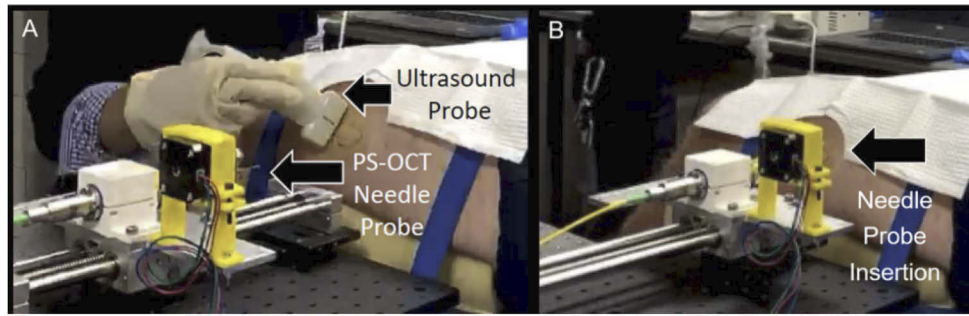


Fig. 2. A) Photo of system/sample arrangement with the leg strapped onto the bench and the area where the needle is to be inserted into the leg sterilized with iodine. An ultrasound probe is used to visualize subsurface tissue. B) The needle probe is attached to the combined translation and rotation stage and inserted into the thigh muscle.

[12]. In short, the Jones-matrices across an entire B-scan are symmetrized by multiplication with a corrective Jones-matrix, thereby removing circular retardation and circular diattenuation that are caused by system elements rather than by the sample [9]. System polarization distortions such as PMD are subsequently removed by multiplication with a wavelength-dependent correction matrix [9]. By analyzing the evolution of the polarization state of the light backscattered from the imaging window of the needle probe over one full rotation, the transmission matrices of the static and rotating system components are found and removed [12], leaving a tomogram of Jones-matrices representing only the sample properties. To suppress speckle and noise in the birefringence measurement, we then convert the 2×2 complex Jones-matrices to 4×4 real-valued Mueller-Jones matrices where each pixel is weighted with its signal intensity before spatial averaging with a two-dimensional Gaussian filter with a 3° angular width and $25 \mu\text{m}$ axial length. Transition from cumulative to local properties is then achieved by following a differential Mueller matrix formalism [10,11,13], using a differential depth of $10 \mu\text{m}$ and thus birefringence and DOP are obtained. The local optic axis orientation is calculated following a recursive peeling algorithm that takes into account the optic axis orientation of preceding layers [9]. As a final note, throughout the manuscript, the authors have displayed local tissue polarization properties such as birefringence and degree of polarization (as color hue) overlaid on structural intensity (as brightness) to facilitate image interpretation. In case of the image showing the tissue optic axis orientation we used birefringence instead of structural intensity as brightness in order to focus the attention on the birefringent tissue.

2.3. Out-of-plane fiber orientation

When propagating in fibrous tissue, polarized light experiences different optical refractive indices depending on the relative alignment between its polarization and the fiber direction (Fig. 3). Specifically, the light experiences the extraordinary refractive index n_e when its polarization is aligned with the fiber, and the ordinary optical refractive index n_o when its polarization is perpendicular to the fiber. The optical birefringence is defined as the difference in optical refractive index: $\Delta n = n_e - n_o$. Measuring the tissue birefringence via the employed Jones-matrix approach with two input states does not require alignment of the actual input polarization states with the tissue fibers in any specific way, except that the beam is perpendicular to the fiber orientation. In the general case of inserting the needle non-perpendicularly through the tissue surface and into tissue of oblique and unknown fiber orientation, the relative angle between the output beam and the tissue fibers is unknown. However, during the rotation of the needle probe, the beam cycles through different beam-fiber angles and the desired perpendicular orientation is

achieved twice per B-scan (see Fig. 3). In this orientation, which is identifiable from its peak birefringence, the measurement represents the true tissue birefringence.

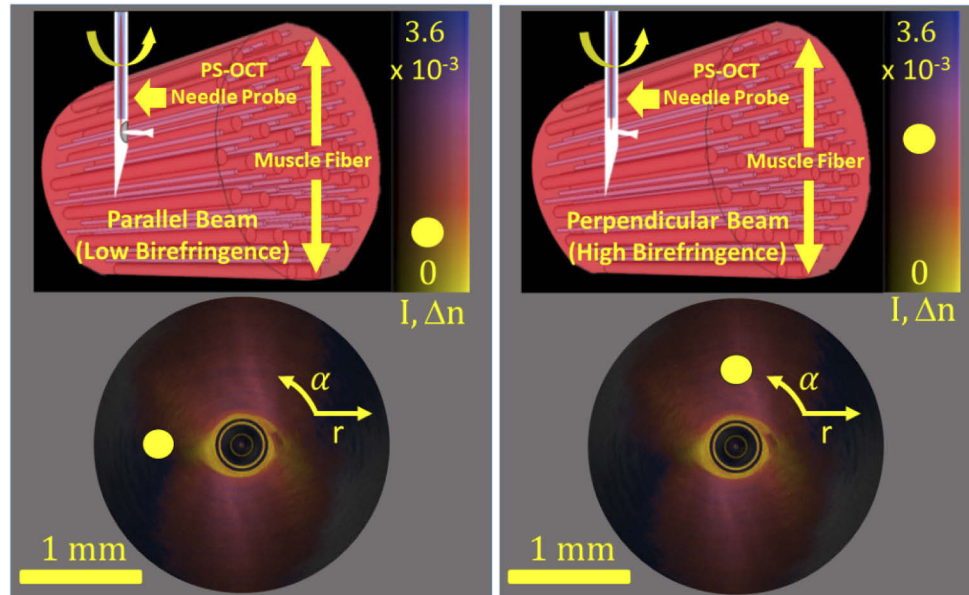


Fig. 3. Representation of needle-muscle imaging geometry. The image on the top left shows a beam pointing parallel to the muscle fibers, experiencing the least birefringence, with the yellow dot in the color bar indicating the amount of birefringence that was measured. The bottom left image is the resulting local birefringence image as a function of rotation. The image on the top right shows a beam pointing perpendicular to the birefringent muscle fibers, with the yellow dot in the color bar indicating the amount of birefringence that can be measured. With the beam point perpendicular to the birefringent muscle fibers the highest birefringence values are observed as shown by a yellow dot in the color bar in the top right and also with a yellow dot in the lower right hand image.

3. Results

3.1. Identification of tissue features in comparison to ultrasound

The deepest recorded PS-OCT images correspond to a depth of 6 mm beneath the dermis as visualized in the 3-dimensional representation of the scan (Fig. 4). The OCT structural images show uniform, striated muscle tissue running roughly east to west in the disk-like cross-sectional image (Fig. 5). The striated appearance is substantially more pronounced in the overlaid intensity/birefringence image, where individual muscle fibers become visible. The straight trajectory of the fibers is disturbed by the presence of the needle itself, causing the muscle fibers to warp outwards, giving the appearance of circumferential orientation. Looking closely however, one can identify the locations (at east and west orientation) of conversion resembling a laminar flow around a circular object. Here the muscle fibers are running radially outwards and hence parallel to the laser beam emitted from the spinning needle probe. Therefore, these regions appear largely void of backscattered light and the muscle fibers appear non-birefringent. The true tissue birefringence can be measured where fibers are running perpendicularly to the beam, at angles near the north and south orientation in the cross-sectional images. The needle in the center of the cross-sectional images features a strong back reflection at its imaging window that appears as a bright circular line accompanied by signal void regions of transparent optical glue / glass. In

the birefringence images, the needle appears surrounded by a lowly birefringent (yellow) but highly scattering and circularly symmetrical layer, which is hypothesized to be a fluid, potentially blood filling the inevitable small gap between needle and tissue.

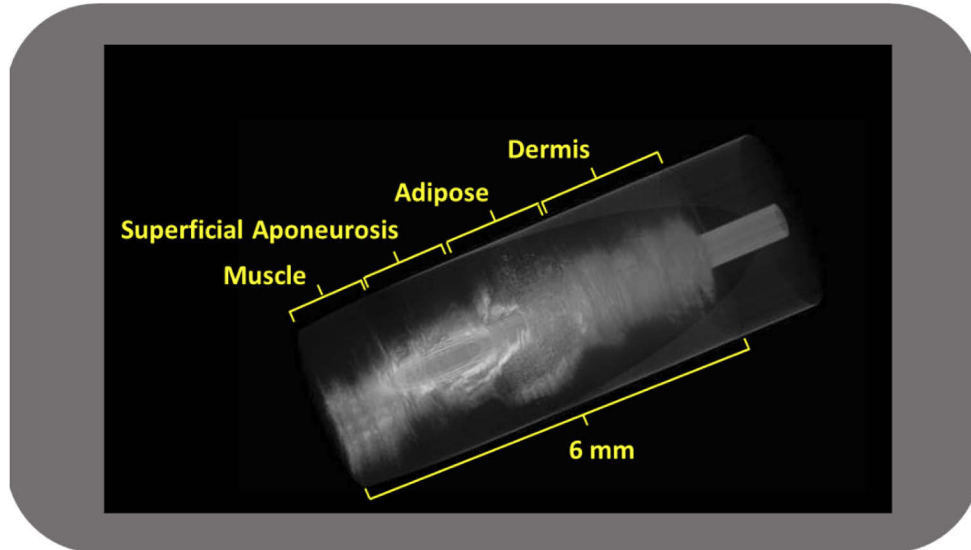


Fig. 4. A 3-dimensional image generated by the PS-OCT needle probe scan with corresponding depths of identified tissue as indicated by overlay with ultrasound imaging.

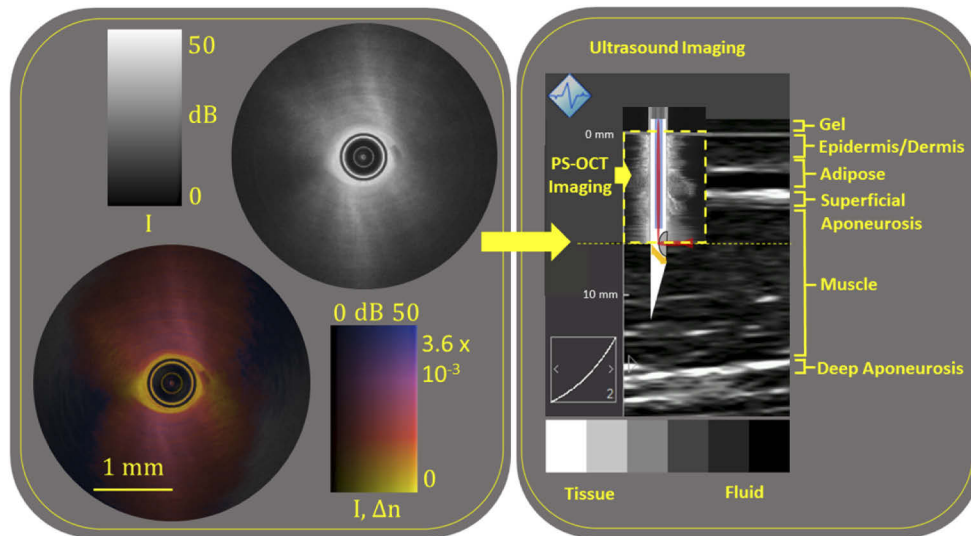


Fig. 5. PS-OCT needle probe and laser beam overlaid on the ultrasound image at depths that were reconstructed from PS-OCT alone. Tissue recognition between PS-OCT and ultrasound imaging of skeletal muscle is apparent.

The muscle tissue is present in the PS-OCT scan between depths of 4.5–6 mm. At 4.5 mm depth a structure of very high birefringence and particular orientation, identified as superficial aponeurosis, gradually becomes visible together with what appears to be adipose tissue with its

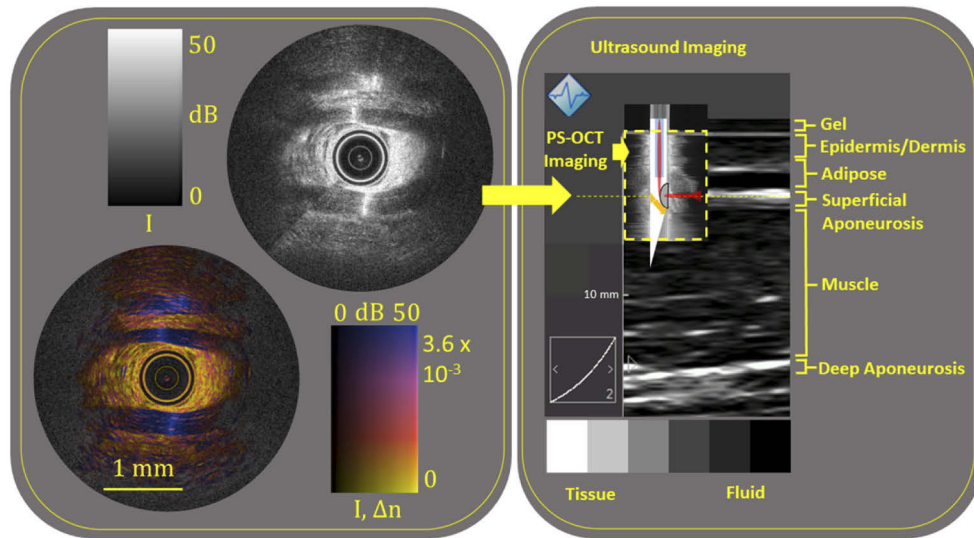


Fig. 6. PS-OCT needle probe and laser beam overlaid on the ultrasound image at depths that were reconstructed from PS-OCT alone. Tissue recognition between PS-OCT and ultrasound imaging of skeletal muscle is apparent.

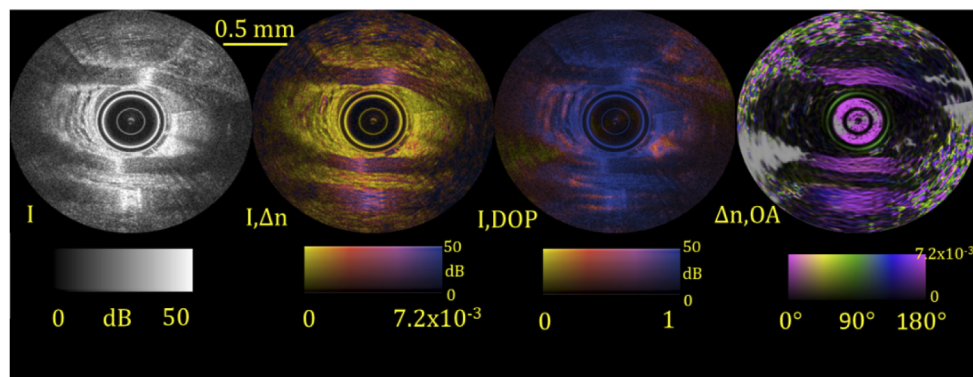


Fig. 7. PS-OCT modalities (intensity, local birefringence, degree of polarization (DOP) and tissue optic axis orientation) of superficial aponeurosis.

characteristic pod-like appearance in the structural OCT image and absent birefringence (Fig. 6). Small individual spots of blue (high birefringence, southwest to southeast) are artefacts from pixels with low intensity and unreliable Mueller matrices.

Eventually, the imaging window of the needle probe is fully seated within the connective tissue of the superficial aponeurosis and multiple highly birefringent band-like structures with definite orientation (east to west, parallel to the projection of the muscle fibers) become visible (Fig. 7, birefringence is scaled differently from muscle images to avoid saturation). The relative orientation of fibrous structures is another parameter that is accessible through the local optic axis orientation. Fig. 7 reveals the uniform orientation of the highly organized superficial aponeurosis. However, PS-OCT derived local birefringence and local optic axis measurements are only reliable where the backscattered light retains a high degree of polarization (DOP). The DOP was close to unity in most of the total scan volume, however regions of depolarizing tissue were occasionally observed.

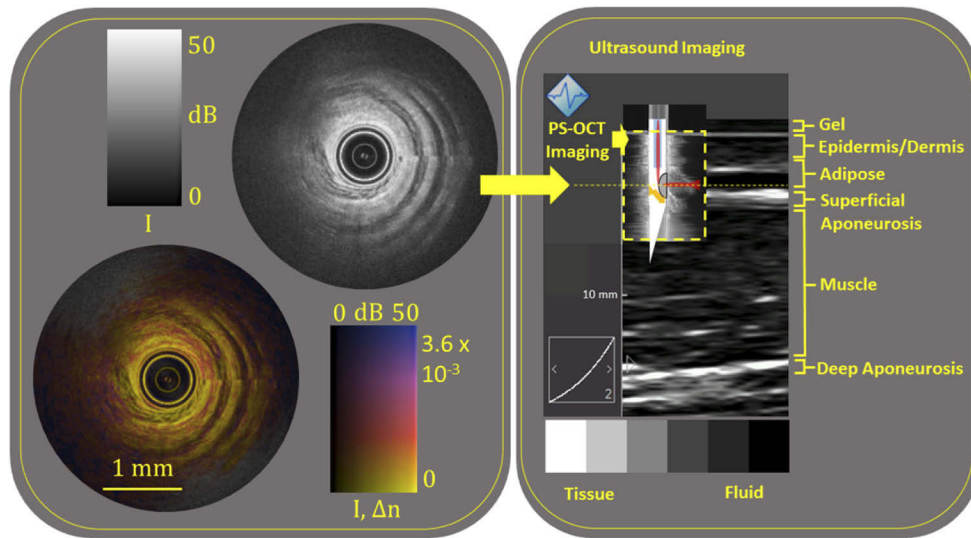


Fig. 8. PS-OCT needle probe and laser beam overlaid on the ultrasound image at depths that were reconstructed from PS-OCT alone. Tissue recognition between PS-OCT and ultrasound imaging of skeletal muscle is apparent.

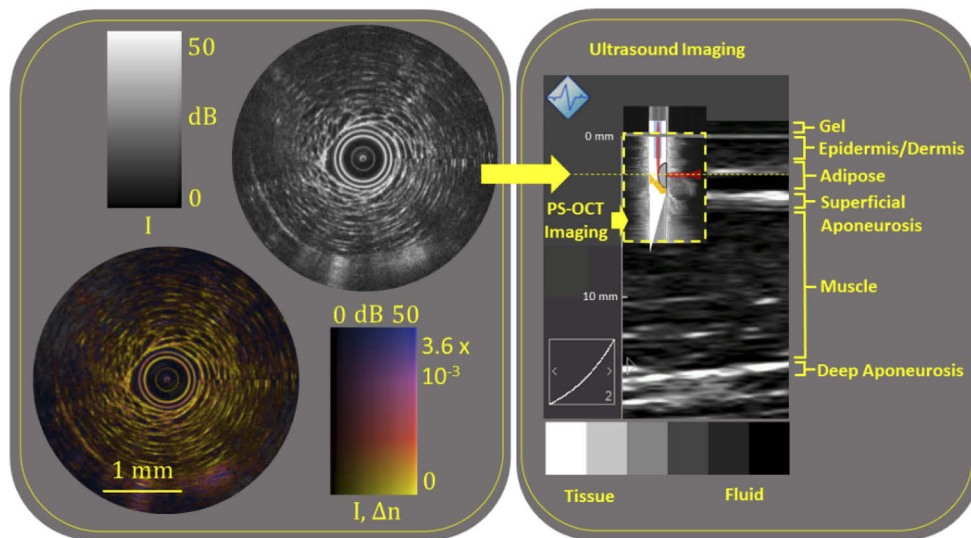


Fig. 9. PS-OCT needle probe and laser beam overlaid on the ultrasound image at depths that were reconstructed from PS-OCT alone. Tissue recognition between PS-OCT and ultrasound imaging of skeletal muscle is apparent.

Superficially to the connective tissue a layered arrangement with lowly-birefringent, homogeneously scattering tissue intersected by layers of adipose tissue becomes visible (Fig. 8). Subsequently, the dominating appearance is that of non-birefringent adipose tissue (Fig. 9) with its characteristic pod structure before the needle was retracted to the epidermis. Observed tissue drag was assessed by comparing B-scans from left- and right-handed rotations (not shown) and was negligible in skeletal muscle but visible in adipose tissue and epidermis/dermis, leading

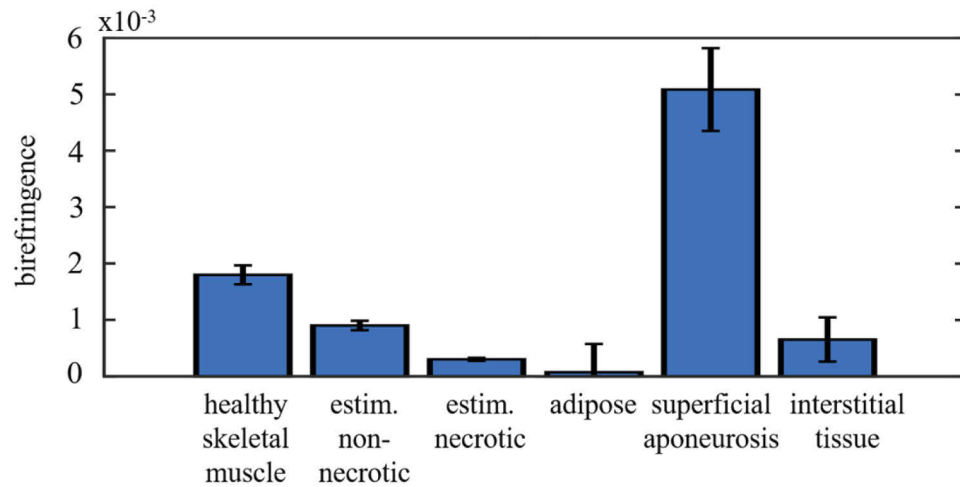


Fig. 10. Quantitative birefringence measurement (mean \pm SD) of various human tissue types. Estimations for reduced birefringence of necrotic and non-necrotic damaged skeletal muscle are assuming a similar percent reduction as that observed in skeletal muscle of *mdx*-mice [5].

to the impression of circumferentially layered tissue in Fig. 8 as well as small image stitching misalignments.

3.2. Quantitative birefringence assessment of human tissues

Scanning a cylindrical volume of 3.5×6 mm (diameter \times length) we measured the mean and standard deviation of birefringence of several distinct tissue types in a healthy subject (Fig. 10). Skeletal muscle birefringence was $\Delta n = 1.79 \times 10^{-3} \pm 0.18 \times 10^{-3}$, adipose $\Delta n = 0.07 \times 10^{-3} \pm 0.50 \times 10^{-3}$, superficial aponeurosis $\Delta n = 5.08 \times 10^{-3} \pm 0.73 \times 10^{-3}$ and interstitial tissue $\Delta n = 0.65 \times 10^{-3} \pm 0.39 \times 10^{-3}$. We estimate the degrading impact of muscular dystrophy by assuming a similar percent reduction of birefringence as in exercise-induced non-necrotic and necrotic damage [5], resulting in $\Delta n = 0.90 \times 10^{-3} \pm 0.09 \times 10^{-3}$ and $\Delta n = 0.30 \times 10^{-3} \pm 0.03 \times 10^{-3}$, respectively.

4. Discussion and conclusion

This investigation has shown that a PS-OCT needle probe can be inserted into *in vivo* human skeletal muscle to calculate birefringence values as an assessment of skeletal muscle structural integrity. Birefringence measurements have been utilized previously to image skeletal muscle structure [1] but never before in live human tissue. Following application of topical anesthetic cream the scans allowed for a pain-free, fast and minimally invasive quantitative imaging for detection of possible pathology. Our quantitative measurements of healthy skeletal muscle ($\Delta n = 1.79 \times 10^{-3}$) agree well with previously published values in different species, such as murine ($\Delta n = 1.9 \times 10^{-3}$) [14], but are substantially larger than that of zebrafish ($\Delta n = 1.1 \times 10^{-3}$) [15], a common model for muscular dystrophy and drug screening [2,16]. The high birefringence of human superficial aponeurosis ($\Delta n = 5.08 \times 10^{-3}$) is larger than in other species such as porcine ($\Delta n = 4.0 \times 10^{-3}$) [17,18] and bovine ($\Delta n = 3.7 \times 10^{-3}$) tendon [19]. To our knowledge these data represent the first *in vivo* birefringence measurement of human skeletal muscle and aponeurosis. As mentioned previously, PS-OCT derived birefringence values are already known to be effective for identification of skeletal muscle structural disruption as a result of muscular dystrophy and

exercise related muscle damage [4,5]. PS-OCT analysis of skeletal muscle structural integrity has now progressed from using excised animal muscle tissue to *in vivo* imaging in the current investigation.

While the measurement uncertainty of the quantitative muscle birefringence was an order of magnitude smaller than the absolute value, it is thinkable that the presence of the needle probe itself impacts the measured birefringence by causing a degree of axial tensioning of the muscle fibers and potentially compressing the needle-adjacent tissue. Such effects would decay with distance from the needle, however, tissue birefringence appeared homogeneous over depth and the measurement error was dominated by local fluctuations that represent small scale variations in tissue properties. We therefore conclude that the presence of the needle does not impair accurate quantitative measurements.

Future research will continue to investigate the viability of this new technique in distinguishing between healthy muscle tissue and tissue affected by exercise and disease. The change in birefringence in the affected muscle compared to the small standard deviation (see Fig. 10) suggests that our method holds sufficient precision to resolve multiple intermediate steps and potentially aid in early detection of muscular dystrophy. In particular, Duchenne Muscular Dystrophy (DMD) is a skeletal muscle pathology by which the genetic code necessary for the transcription of the protein dystrophin is absent. Dystrophin is a vital structure that binds the muscle contractile matrix to the cell membrane (sarcolemma). DMD occurs in roughly 1 in 5,000 births with the disproportionate amount occurring in males. Life expectancy ranges from 23 to 30 years of age. Symptoms can appear as early as 3 years old and are marked by a profound progressive loss of muscle strength and power. Mobility is affected early in the progression of the disease, as capabilities of the muscles of the hips and legs decrease. Muscle function degenerates over time due to the important role of dystrophin in lateral force transfer within muscle fibers. This 427 kDa protein is instrumental to proper Z-line function which translates lateral muscular stability into functional force production of the muscle [20].

Current methods of DMD diagnosis are limited and very invasive. Progressive asymmetrical muscle weakness identification and elevated blood creatine kinase levels are more simple diagnosis tools but are not specific to DMD. Bergstrom needle muscle biopsies can be analyzed through immunohistochemistry to identify the level of dystrophin within the muscle [21]. However, Bergstrom needle muscle biopsies are a highly invasive procedure and analysis either through histology or atomic force microscopy can be very costly and time consuming (several days or weeks depending on hospital lab capabilities) [22]. The Bergstrom needle muscle biopsy can be painful and involves locally injected lidocaine for pain, a 1-2 cm scalpel incision in the leg and then a large biopsy needle (5 mm) inserted into the incision [23]. A sliding trap door guillotine mechanism with suction supplied via a manually operated syringe is employed for the muscle tissue extraction [23]. In stark contrast, the PS-OCT needle probe imaging process used in this investigation involves only topical lidocaine and a very small 0.57 mm needle (24-gauge), similar to a typical needle for clinical blood draws. Images can be obtained within 10 minutes and analysis automated and occur within several minutes or even in real-time.

The use of a PS-OCT needle probe to differentiate between health and dystrophin deficient skeletal muscle has been clearly shown in mice [4]. These patterns are unique to DMD, only appearing otherwise after intense eccentric exercise. Birefringence values obtained during PS-OCT scans also specifically identify the regions within the muscle that are dystrophin deficient. Therefore, this allows for repeated measure and tracking of progression of DMD over time. Although PS-OCT technique can be considered minimally invasive, which makes probing of multiple locations feasible, it should be noted that only a relatively small cylindrical volume of 3.5×6 mm (diameter x length) was probed in the current study. The pullback distance can simply be extended to several centimeters by a deeper insertion of the needle. Due to the similarity of skeletal muscle throughout the body we suggest that exercise-induced damage may

be quantified in a single session by comparing skeletal muscle from frequently activated and more passive regions to derive an individual integrity score. Where repeated necrotic events cause replacement of skeletal muscle tissue with fibrotic connective and adipose tissue [24], these changes can be monitored with PS-OCT. As previously mentioned, to make the PS-OCT technology practical and to give clinicians quick access to the results, much of the data processing can be automated and performed live. Note that such quick access will be an advantage of this technology over the Bergstrom needle muscle biopsies which are currently taken, as they do not require extensive histological processing. Finally, this expeditious and economical minimally invasive and pain-free approach opens up the possibility of low threshold clinical studies. In conclusion, the current investigation has shown that examination of human skeletal muscle *in vivo* utilizing a PS-OCT needle probe is feasible and yields valuable data concerning anatomical structure and integrity.

Funding. Ministry of Science and ICT, South Korea (2019H1D3A2A02101784); National Health and Medical Research Council (APP1180854).

Acknowledgements. The authors acknowledge helpful discussions with Dr. Dirk Lorenzer (Cylite HP-OCT) and Professor Robert McLaughlin (University of Adelaide).

Disclosures. The authors declare no conflicts of interest.

Data availability. Data underlying the results presented in this paper are not publicly available at this time but may be obtained from the authors upon reasonable request.

References

1. R. C. Haskell, F. D. Carlson, and P. S. Blank, "Form Birefringence of Muscle," *Biophys. J.* **56**(2), 401–413 (1989).
2. H. Lodish, A. Berk, C. A. Kaiser, M. Krieger, A. Bretscher, H. Ploegh, K. C. Martin, M. B. Yaffe, and A. Amon, *Molecular cell biology* (Macmillan Learning, 2021).
3. J. Berger, T. Sztal, and P. D. Currie, "Quantification of birefringence readily measures the level of muscle damage in zebrafish," *Biochem. Biophys. Res. Commun.* **423**(4), 785–788 (2012).
4. X. J. Yang, L. X. Chin, B. R. Klyen, T. Shavlakadze, R. A. McLaughlin, M. D. Grounds, and D. D. Sampson, "Quantitative assessment of muscle damage in the mdx mouse model of Duchenne muscular dystrophy using polarization-sensitive optical coherence tomography," *J. Appl. Physiol.* **115**(9), 1393–1401 (2013).
5. X. J. Yang, D. Lorensen, R. A. McLaughlin, R. W. Kirk, M. Edmond, M. C. Simpson, M. D. Grounds, and D. D. Sampson, "Imaging deep skeletal muscle structure using a high-sensitivity ultrathin side-viewing optical coherence tomography needle probe," *Biomed. Opt. Express* **5**(1), 136–148 (2014).
6. R. A. McLaughlin, B. C. Quirk, A. Curatolo, R. W. Kirk, L. Scolaro, D. Lorensen, P. D. Robbins, B. A. Wood, C. M. Saunders, and D. D. Sampson, "Imaging of Breast Cancer With Optical Coherence Tomography Needle Probes: Feasibility and Initial Results," *IEEE J. Sel. Top. Quantum Electron.* **18**(3), 1184–1191 (2012).
7. X. D. Li, C. Chudoba, T. Ko, C. Pitris, and J. G. Fujimoto, "Imaging needle for optical coherence tomography," *Opt. Lett.* **25**(20), 1520–1522 (2000).
8. L. Scolaro, D. Lorensen, R. A. McLaughlin, B. C. Quirk, R. W. Kirk, and D. D. Sampson, "High-sensitivity anastigmatic imaging needle for optical coherence tomography," *Opt. Lett.* **37**(24), 5247–5249 (2012).
9. Q. Li, K. Karnowski, P. B. Noble, A. Cairncross, A. James, M. Villiger, and D. D. Sampson, "Robust reconstruction of local optic axis orientation with fiber-based polarization-sensitive optical coherence tomography," *Biomed. Opt. Express* **9**(11), 5437–5455 (2018).
10. M. Villiger and B. E. Bouma, "Practical decomposition for physically admissible differential Mueller matrices," *Opt. Lett.* **39**(7), 1779–1782 (2014).
11. M. Villiger, D. Lorensen, R. A. McLaughlin, B. C. Quirk, R. W. Kirk, B. E. Bouma, and D. D. Sampson, "Deep tissue volume imaging of birefringence through fibre-optic needle probes for the delineation of breast tumour," *Sci. Rep.* **6**(1), 28771 (2016).
12. M. Villiger, B. Braaf, N. Lippok, K. Otsuka, S. K. Nadkarni, and B. E. Bouma, "Optic axis mapping with catheter-based polarization-sensitive optical coherence tomography," *Optica* **5**(10), 1329–1337 (2018).
13. R. Ossikovski, "Differential matrix formalism for depolarizing anisotropic media," *Opt. Lett.* **36**(12), 2330–2332 (2011).
14. J. J. Pasquesi, S. C. Schlachter, M. D. Boppart, E. Chaney, S. J. Kaufman, and S. A. Boppart, "In vivo detection of exercise-induced ultrastructural changes in genetically-altered murine skeletal muscle using polarization-sensitive optical coherence tomography," *Opt. Express* **14**(4), 1547–1556 (2006).
15. D. Yang, M. Y. Hu, M. Y. Zhang, and Y. M. Liang, "High-resolution polarization-sensitive optical coherence tomography for zebrafish muscle imaging," *Biomed. Opt. Express* **11**(10), 5618–5632 (2020).
16. G. Kawahara, J. A. Karpf, J. A. Myers, M. S. Alexander, J. R. Guyon, and L. M. Kunkel, "Drug screening in a zebrafish model of Duchenne muscular dystrophy," *Proc. Natl. Acad. Sci. U. S. A.* **108**(13), 5331–5336 (2011).

17. L. X. Chin, X. J. Yang, R. A. McLaughlin, P. B. Noble, and D. D. Sampson, "En face parametric imaging of tissue birefringence using polarization-sensitive optical coherence tomography," *J. Biomed. Opt.* **18**(6), 066005 (2013).
18. A. V. Smolensky, J. Ragozzino, S. H. Gilbert, C. Y. Seow, and L. E. Ford, "Length-dependent filament formation assessed from birefringence increases during activation of porcine tracheal muscle," *J. Physiol-London* **563**(2), 517–527 (2005).
19. J. F. de Boer, T. E. Milner, M. J. van Gemert, and J. S. Nelson, "Two-dimensional birefringence imaging in biological tissue by polarization-sensitive optical coherence tomography," *Opt. Lett.* **22**(12), 934–936 (1997).
20. S. Le, M. Yu, L. Hovan, Z. Zhao, J. Ervasti, and J. Yan, "Dystrophin as a molecular shock absorber," *ACS Nano* **12**(12), 12140–12148 (2018).
21. M. Fanin, G. A. Danieli, M. Cadaldini, M. Miorin, L. Vitiello, and C. Angelini, "Dystrophin-positive fibers in Duchenne dystrophy: origin and correlation to clinical course," *Muscle Nerve* **18**(10), 1115–1120 (1995).
22. R. W. van Zwieten, S. Puttini, M. Lekka, G. Witz, E. Gicquel-Zouida, I. Richard, J. A. Lobrinus, F. Chevalley, H. Brune, G. Dietler, A. Kulik, T. Kuntzer, and N. Mermod, "Assessing dystrophies and other muscle diseases at the nanometer scale by atomic force microscopy," *Nanomedicine* **9**(4), 393–406 (2014).
23. R. A. Shanely, K. A. Zwetsloot, N. T. Triplett, M. P. Meaney, G. E. Farris, and D. C. Nieman, "Human skeletal muscle biopsy procedures using the modified Bergstrom technique," *J. Vis. Exp.* **91**, 51812 (2014).
24. H. G. Radley, A. De Luca, G. S. Lynch, and M. D. Grounds, "Duchenne muscular dystrophy: focus on pharmaceutical and nutritional interventions," *Int. J. Biochem. Cell Biol.* **39**(3), 469–477 (2007).